Modeling the Evolution of the Dislocation Density and Yield Stress of Al over a Wide Range of Temperatures and Strain Rates

ABBAS SADEGHI and ERNST KOZESCHNIK

This paper introduces an extended model for the evolution of internal and wall dislocation densities in pure aluminum during plastic deformation. The approach takes the three internal state variables (3IVM) model as a starting point and advances it by taking into account the dynamic annihilation of immobile/locked dislocations as well as dislocations stored in the subgrain/cell walls. The strength of the material, as one of the properties affected by dislocation density, is used to validate the model. Experimental flow curves for pure Al are taken as the basis for calibration. Compression tests are performed at temperatures from $-196\ °C$ to $500\ °C$ with strain rates of 1, 0.1, and 0.01 s^{-1}. The effect of temperature and strain rate on each state parameter is illustrated and discussed.

I. INTRODUCTION

SEVERAL approaches are reported in the literature that aim to describe the flow curves of metallic materials in different stages of deformation. In one group of models, the flow curves of aluminum are simulated without direct consideration of the underlying microstructure,[1–6] with the drawback that they often cannot consider sequences of thermo-mechanical treatments with arbitrary loading and unloading cycles as well as temperature changes.

The present work focuses on a state parameter-based approach that relies on the knowledge of the material microstructure. There exists a vast literature in this field. Tabourot et al.[7] proposed a model that evaluates the dislocation density evolution to capture the behavior of single crystal fcc metals. Kocks[8] accounted for the various stages of plastic deformation and introduced equations to describe flow curves of metals at different temperatures and strain rates within stage III hardening. This approach considers the generation and annihilation of dislocations into the total dislocation density. It is extended and reviewed by Kocks and Mecking.[9] With a focus on Al alloys, Puchi[10] and Abo-Elkhier[11] extended the method from Kocks for predicting flow curves. In both works, the temperature where deformation occurs is higher than 200 °C. Khan et al.[12] compared the compression flow curves for single-crystal aluminum with two models; the classical hardening law and the dislocation density-based model. The dislocation density-based model is more accurate, and it has many parameters. Still, most parameters have physical meaning, and literature exists for a deeper analysis of these. Several other methods based on constitutive equations are summarized and discussed in References 13–20.

All before-mentioned models are founded on one mean total dislocation density for calculations. More advanced methods also exist that describe the metallic microstructure based on different types of dislocations. Kubin and Estrin[21,22] used mobile and forest dislocations to propose a model for plastic deformation that could simulate the Portevin–Le Chatelier effect in aluminum. Barlat et al.[23] developed a model based on mobile and forest dislocations to evaluate the strain rate-dependent hardening of aluminum. These authors considered the average length, that a dislocation moves freely (mean free path), as depending on the dislocation densities. Hansen et al.[24] categorized dislocations as mobile, pile-up, and debris, each characterized by a different potential for mobility. Li and Huang[25] proposed a dislocation-bow-out model and provided quantities on physical basis for the strain rate sensitivity of the Kocks model. Flow curves of aluminum deformed from 100 K to 400 K, with strain rates from 10^{-2} to $10^{-4}\ s^{-1}$, were measured to validate their model. Arsenlis and Parks[26] separated screw and edge dislocations and estimated the effect of each gliding system on the strengthening of aluminum. Goerdeler and Gottstein[27]

ABBAS SADEGHI and ERNST KOZESCHNIK are with the Institute of Materials Science and Technology, TU Wien, Getreidemarkt 9, 1060 Vienna, Austria. Contact e-mail: abbas.sadeghi@tuwien.ac.at

simulated the flow curves of pure aluminum based on the 3IVM model. Their treatment is only strictly valid at higher temperatures because mobile dislocations are considered to be solely edge dislocations.

Nowadays, it is possible to distinguish between wall and internal dislocations experimentally, and each has a different effect on the material properties.[28–31] Numerous work-hardening models were reported in References 32–40. The present work starts with the 3IVM model introduced by Goerdeler and Gottstein[27] as a basis and advances it by introducing additional equations for the dynamic annihilation of immobile and wall dislocations. The new equations make it possible to simulate flow curves in different stages of plastic deformation with a particular focus on higher strains. All equations that are presented in the following Modeling section, have been incorporated into the thermokinetic software Mat-Calc[41] (version 6.04.1004) by one of the authors as a new module for substructure evolution. This software is then used to generate the results of the present manuscript.

Compression tests on pure aluminum are performed to validate the simulation results. Experiments are performed from − 196 °C to 500 °C with strain rates of 1, 0.1, and 0.01 s^{-1}. Good agreement is found between experimental results and simulations based on only one single set of simulation input parameters for all combinations of strain rate and temperature.

II. MODELING

The yield stress of a polycrystalline metallic material can be expressed as a superposition of the initial (thermal) yield stress σ_0 and the plastic (athermal) stress σ_P as

$$\sigma = \sigma_0 + \sigma_P. \qquad [1]$$

The initial yield stress consists of low-temperature and high-temperature parts, and it requires the consideration of thermal activation. However, it is not further treated here because the present focus is on the athermal stress contribution only, which stems from dislocation–dislocation interactions. Details on the thermally activated part are given in, e.g., Kreyca and Kozeschnik.[18] For calculating the plastic stress, which is the work-hardening part of the total strength, an extended version of the Taylor and Orowan equation[42,43] is used with

$$\sigma_P = \alpha_i c_i M G b \sqrt{\rho_i} + \alpha_w c_w M G b \sqrt{\rho_w}. \qquad [2]$$

α_i and α_w are the strengthening coefficients for internal and wall dislocations, respectively, c_i is the volume fraction of cell interiors, c_w is the volume fraction of cell walls, M is the Taylor factor, G is the shear modulus, and b is the Burgers vector. ρ_i is the internal dislocation density, which is the density of dislocations inside the subgrains/cells, and ρ_w represents the average density of wall dislocations, i.e., the accumulated and stored dislocations inside the subgrain walls, or cell walls. Figure 1 illustrates the constitution of the assumed

microstructure. Walls are high-dislocation density areas that enclose low-dislocation density cells; both cells and walls consist of mobile and immobile dislocations.[44] The current model treats the wall dislocations as an excess over the internal dislocations. As described in several previous works,[27,45–48] wall dislocations are constituted mainly by dipoles. Mobile dislocations can move and accommodate plastic deformation, whereas immobile dislocations and dipoles do not contribute to plastic deformation.

A. Generation of Dislocations

The plastic deformation of metallic materials is carried by the generation and movement of mobile dislocations. Their generation rate, $\dot{\rho}_m^+$, is commonly written as[9,44,49]

$$\dot{\rho}_m^+ = \frac{M\dot{\varepsilon}}{bL_{eff}}, \qquad [3]$$

where $\dot{\varepsilon}$ is the strain rate, and L_{eff} is the effective travel distance of a dislocation before it becomes arrested in a subgrain boundary or immobilized in the cell interior. Various microstructural features can act as obstacles for mobile dislocations. Among them are grain boundaries and other mobile, immobile, or wall dislocations. A common way to express the effective travel distance is[27,44,45]

$$\frac{1}{L_{eff}} = \frac{\sqrt{\rho_i}}{A_m} + \frac{\sqrt{\rho_w}}{\beta_w} + \frac{\beta}{D}, \qquad [4]$$

where A_m is a parameter describing the contribution of internal dislocations to the mean free path. β_w and β are fitting parameters related to the wall dislocations and the grain size, and D is the grain diameter.

B. Dynamic Recovery of Dislocations

1. Critical volume
During deformation, mobile dislocations can annihilate, become immobile, or form dipoles that aggregate as wall dislocations. A continuous generation of all three dislocation types persists. The present work assumes that mobile dislocations interact with other dislocations when they come close enough to each other and the elastic stress fields overlap sufficiently.

The strength of the elastic stress field is inversely proportional to the distance from the dislocation line and a critical distance (d_c) from a dislocation line exists, within interactions are possible. This distance has been calculated as[50]

$$d_c = \frac{Gb^4}{2\pi(1 - \nu)Q_{va}}, \qquad [5]$$

where ν is the Poissions ratio and Q_{va} is the vacancy formation energy. The critical volume for interaction can be defined as the swept volume spanned by the critical interaction distance, the distance that the mobile dislocation travels, and the unit length of a dislocation in the third spatial dimension. A sketch of this volume is
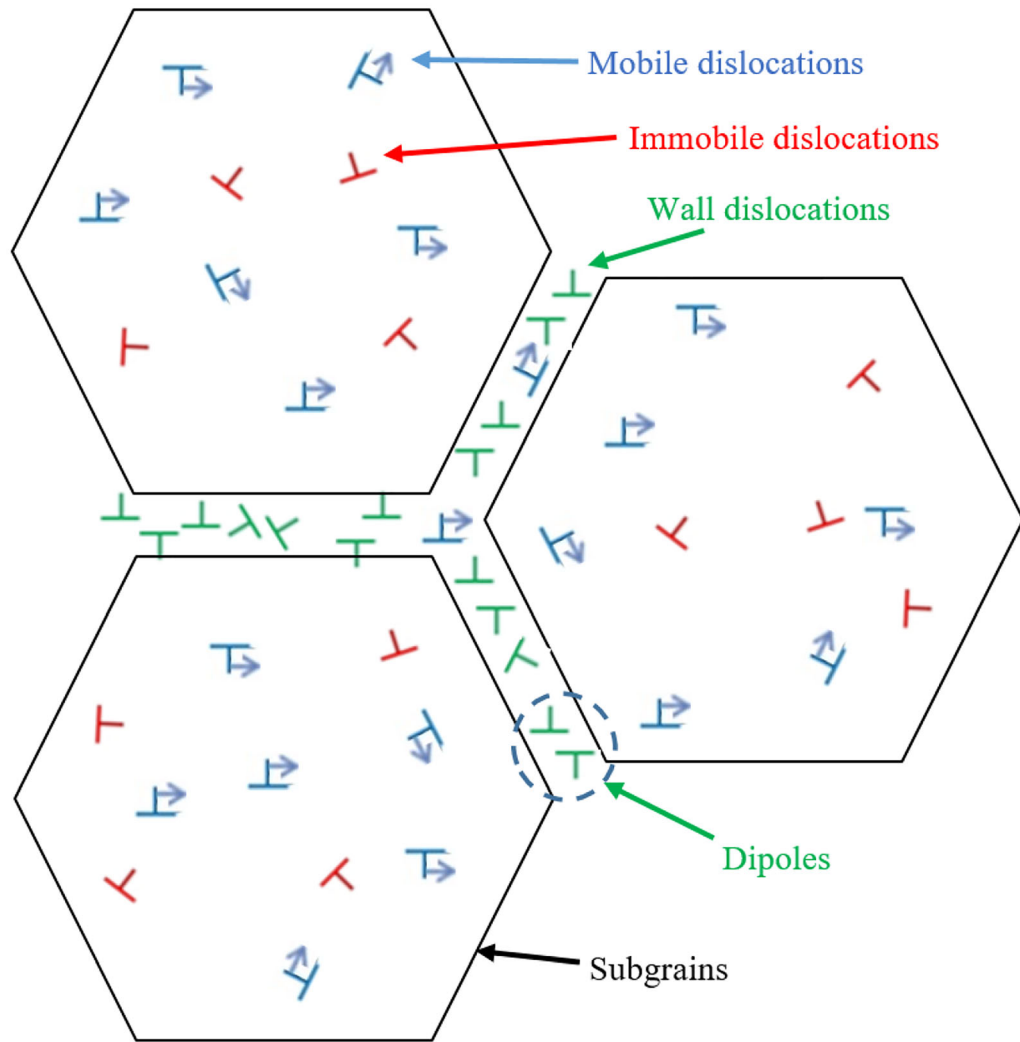
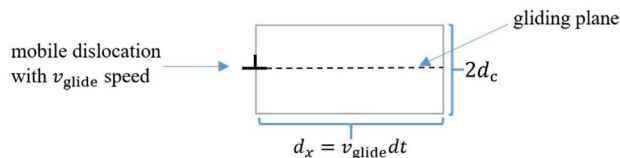Fig. 1—Schematic illustration of dislocation arrangement during deformation.

Fig. 2—Swept volume by a mobile dislocation, which is critical for interaction.

shown in Figure 2. This volume can be calculated with the approach introduced by Friedel.[50] A mobile dislocation with the velocity v_{glide} sweeps a volume of $2 \cdot 1m \cdot d_c v_{glide} dt$ during a dt time increment.

The total length of mobile dislocations in a unit volume is equal to ρ_m, where ρ_m denotes the average density of mobile dislocations inside the grains. Therefore, the total swept volume, V, by all mobile dislocations in a unit volume during a unit time ($dt = 1$) can be written as

$$V = 2d_c v_{glide} \rho_m.$$ [6]

With the Orowan equation,[51]

$$M\dot{\varepsilon} = b v_{glide} \rho_m,$$ [7]

the critical interaction volume is, finally,

$$V = 2 \frac{M\dot{\varepsilon}}{b} d_c.$$ [8]

As mentioned before, one part of any interaction is a mobile dislocation, which defines the critical interaction volume. The other partner can be a dislocation of any type (mobile, immobile, and wall) within this volume. Different interactions are possible based on the second partner, which is further elaborated in the following sections.

2. *Mobile–mobile interactions*
Dislocations and their interactions are complex, and a simplified method of interactions between dislocation lines or part of them is outlined here. More information
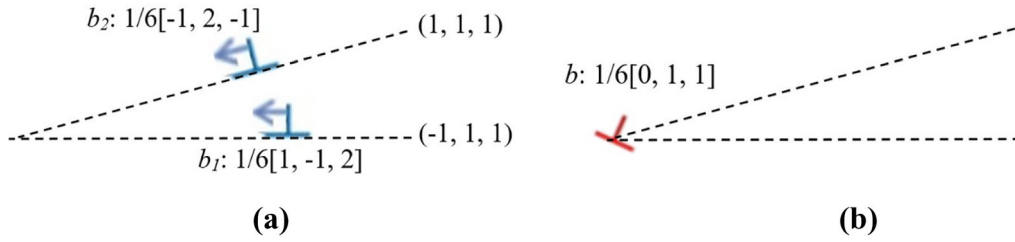
Fig. 3—Example of an immobile dislocation, which is created from data in Reference 52, showing how two mobile dislocations in different gliding systems (*a*) interact and create one immobile dislocation (*b*).

about interactions can be found in, *e.g.*, References 50, 52.

For annihilation, two mobile dislocations in a similar glide system and opposite directions must come close enough to each other to interact. For the transformation of mobile dislocations into immobile ones, the two dislocations must interact and create a dislocation with a resulting Burgers vector that points into a direction outside a glide system. Figure 3 shows an example of corresponding interactions.[52]

Two mobile dislocations in opposite directions and similar gliding planes attract each other, and the most stable position is when they lie above each other, as shown in Figure 4.[52] If the distance of the two dislocations is not close enough to cause annihilation, but still close enough to interact, this pair of dislocations is called a dipole, which commonly aggregates to form subgrain/cell walls.[46] Details on forming walls during plastic deformation and their dislocations are given in Reference 50.

It is worth mentioning that all the before-mentioned interactions are examples of mobile–mobile dislocation interactions. In general, different interactions can result in the annihilation of mobile dislocations with a probability factor of B, in turning into immobile dislocations inside the subgrain/cell with a probability of A_{imm}, or turning into wall dislocations with a probability of A_w. Details on the calculations are described in Reference 44. The equation for annihilation, as used in the present work, reads

$$\dot{\rho}_{m,ann}^{-} = B \cdot V \cdot \rho_{m}, \qquad [9]$$

the equation for turning mobile into immobile dislocations inside the subgrain/cell is

$$\dot{\rho}_{m,imm}^{-} = \dot{\rho}_{imm}^{+} = 2A_{imm} \cdot V \cdot \rho_{m}, \qquad [10]$$

and the equation for turning mobile dislocations into wall dislocations is

$$\dot{\rho}_{m,w}^{-} = f_{w} \cdot \dot{\rho}_{w}^{+} = A_{w} \cdot V \cdot \rho_{m}. \qquad [11]$$

The generation rate of immobile dislocations is denoted as $\dot{\rho}_{imm}^{+}$, and the generation rate of wall dislocations is denoted as $\dot{\rho}_{w}^{+}$.
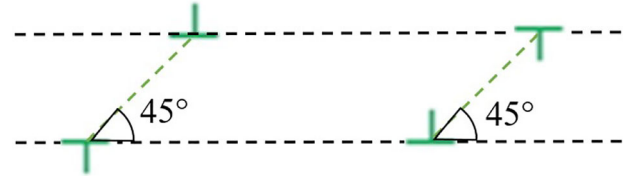

Fig. 4—Dipoles formed by two mobile dislocations in similar gliding planes, which is created from data in Reference 52.

3. Mobile–immobile and mobile–wall interactions

In the present model, immobile and wall dislocations are assumed to interact with mobile dislocations such that they potentially annihilate. This assumption is rather generic, or phenomenological, since no specific interaction mechanism is imposed, except that the interaction rate can be described by the critical interaction volume. The number of interaction partners for mobile dislocations is defined by the density of immobile and wall dislocations inside the critical interaction volume. For the annihilation of immobile dislocations, the number of interaction partners is

$$N_{imm} = V \cdot \rho_{imm}, \qquad [12]$$

and the number of interaction partners for the annihilation of wall dislocations is

$$N_{w} = V \cdot \rho_{w}, \qquad [13]$$

where ρ_{imm} denotes the average density of immobile dislocations in subgrains/cells. With the probabilities for interaction, the annihilation rates of immobile and wall dislocations can be written as

$$\dot{\rho}_{imm}^{-} = B_{imm} \cdot V \cdot \rho_{imm} \qquad [14]$$

and

$$\dot{\rho}_{w}^{-} = B_{w} \cdot V \cdot \rho_{w}. \qquad [15]$$

B_{imm} and B_{w} are related to the probabilities of annihilating immobile and wall dislocations, respectively.

C. Static Recovery of Dislocations

In addition to the plastic deformation-induced mechanisms described in the previous section, dislocations can interact and annihilate by climbing. No explicit deformation is required for these processes, which is why they are commonly denoted as static recovery. According to Lagneborg et al.,[53,54] for the static annihilation of mobile dislocations, the following rate equation can be used

$$\dot{\rho}_m^- = 2C_m \frac{DGb^3}{kT}\left(\rho_m{}^2 - \rho_{equ,m}^2\right), \qquad [16]$$

where C_m is a calibration parameter, k is the Boltzmann constant, and $\rho_{equ,m}$ is the equilibrium density of mobile dislocations. In the current study, D is the effective bulk diffusion coefficient, which, for n substitutional elements, reads[55]

$$D = \sum_{i=1}^{n} D_i y_i. \qquad [17]$$

D_i is the tracer diffusion coefficient of substitutional element i and y_i is the site fraction of the respective element. More details are reported in Fischer et al.[55] For the wall and immobile dislocations, analogous equations are used in the model, with separate coefficients C_{imm} and C_w.

Finally, the relevant equation for mobile dislocations is

$$\dot{\rho}_m = \frac{M\dot{\varepsilon}}{b\left(\frac{\sqrt{\rho_i}}{A_m} + \frac{\sqrt{\rho_w}}{\beta_w} + \frac{\beta}{D}\right)}$$
$$- (B \cdot V \cdot \rho_m + 2A_{imm} \cdot V \cdot \rho_m + A_w \cdot V \cdot \rho_m)$$
$$- 2C_m \frac{DGb^3}{kT}\left(\rho_m{}^2 - \rho_{equ,m}^2\right), \qquad [18]$$

for immobile dislocations

$$\dot{\rho}_{imm} = 2A_{imm} \cdot V \cdot \rho_m - B_{imm} \cdot V \cdot \rho_{imm}$$
$$- 2C_{imm} \frac{DGb^3}{kT}\left(\rho_{imm}{}^2 - \rho_{equ,imm}^2\right), \qquad [19]$$

and for wall dislocations

$$\dot{\rho}_w = \frac{1}{f_w} A_w \cdot V \cdot \rho_m - B_w \cdot V \cdot \rho_w$$
$$- 2C_w \frac{DGb^3}{kT}\left(\rho_w{}^2 - \rho_{equ,w}^2\right). \qquad [20]$$

D. Simulation

Compression tests up to a true strain of 0.8 are performed to assess the capabilities of the model. In each simulation, the evolution of dislocation densities is calculated as a function of strain, strain rate, and temperature, and related to the measured flow curve. The simulations are performed with the thermokinetic software MatCalc,[41] which incorporates the model that

has been described before. Table I summarizes the material input parameters.

III. EXPERIMENTAL

An aluminum cylinder with a diameter of 76 mm and a purity of 99.999 pct from HMW Hauner company is used. Figure 5 shows its microstructure in transverse and longitudinal cross-sections provided by light microscopy and color etching. Cylindrical samples parallel to the original cylinder are machined with a length of 10 mm and a diameter of 5 mm and deformed at three different strain rates of 1, 0.1, and 0.01 s^{-1}. The compression tests are performed at temperatures between -196 °C and 500 °C. Table II shows used strain rates and temperatures. Liquid nitrogen and a mixture of acetone and dry ice are used to achieve -196 °C and -50 °C, respectively. Cooling liquids are poured directly on samples during the tests. The tests are performed on the dilatometer DIL 805 A/D manufactured by Baehr using graphite as a lubricant to prevent barreling.

IV. RESULTS

The exemplary simulation results for 0.1 s^{-1} strain rate at three different temperatures are shown in Figure 6. The strength of the material is calculated from Eq. [2] with the simulated wall dislocation density (red dashed line) and the internal dislocation density (magenta dashed line). The calculated strength is compared with the experimental results from compression tests. As highlighted before, it is possible to simulate flow curves at higher strain with the new annihilation equations (14) and (15)

The simulation results in Figure 6 show that the mobile dislocation density increases fast at the beginning of the deformation, and immobile and wall dislocations are generated only after the density of mobile ones increases sufficiently. Also, it shows that the reduction rate is more noticeable for mobile dislocations than for immobile and wall dislocations. Another point from simulations is that the ratio of the wall or immobile dislocation density to mobile dislocation density increases with increasing temperature.

A comparison between the simulated dislocation density and experimental results from Gubicza et al.[65] and Chinh et al.[66] is shown in Figure 7. Gubicza et al. measure the dislocation density of 4N purity (99.99 pct) aluminum with X-ray diffraction. Chinh et al. simulate the dislocation density based on the results of tensile and compression tests for a 4N purity aluminum. Since 5N purity aluminum is used in the current work, the dislocation density is slightly smaller. Otherwise, the present simulations agree well with their results.

In the practical analysis, each experimental flow curve is first fitted individually with the parameters of the model. Each parameter is then plotted as a function of temperature and strain rate. Finally, a function for each parameter is evaluated that represents the observed

Symbol	Name	Value	Unit	Literature Source
v	Poisson's ratio	0.347	—	[56]
G	shear modulus	$29,438.4 - 15.052T$	MPa	[57, 58]
M	Taylor factor	3.06	—	[59, 60]
b	length of Burgers vector	2.86×10^{-10}	m	[49, 61]
Q_{va}	Vacancy formation energy	0.642	eV	[62–64]
c_w	volume fraction of cell walls	0.1	—	[44]
c_i	volume fraction of cell interior	0.9	—	[44]
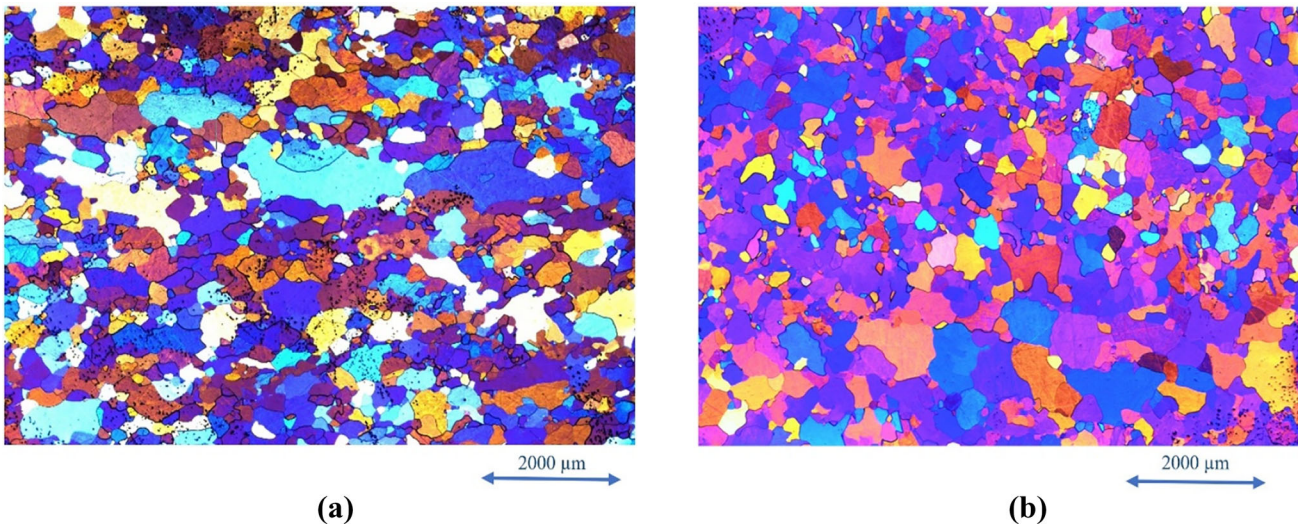
Fig. 5—The microstructure of the as-received pure Al provided by color etching in (*a*) transverse cross-section and (*b*) longitudinal cross-section (Color figure online).

Table II.   Selected Strain Rates and Temperatures

Strain rates (s^{-1})	Temperatures (°C)
1	-196
	-50
0.1	30
	100
0.01	300
	500

temperature- and strain rate-dependency. Table III summarizes the calibration parameters and optimized functions.

The results of simulations with the proposed functions are shown in Figure 8. For comparison, the results from experimental tests are displayed simultaneously. For better illustration, the initial part of the flow curves is augmented on the left side of each plot. The simulation agrees well with the experimental results in different stages of deformation.

V.   DISCUSSION

The evaluation of dislocation densities in Figure 6 shows that mobile dislocations are generated rapidly and soon reach a plateau. Mobile dislocations accommodate plastic deformation and any change in their density comes from the balance of generation, annihilation, and transformation into immobile or wall dislocations. The mechanisms that reduce the mobile dislocation density come from dislocation interactions, which are directly dependent on the mobile dislocation density. At the beginning of deformation, the mobile dislocation density is low, and only a small number of mobile dislocations interact. Therefore, the generation of mobile dislocations is dominant at the beginning of deformation. With increasing strain, interactions become more probable, making the reduction mechanisms more prominent. After a characteristic amount of deformation, the mobile dislocation density reaches a plateau, which marks the point where the generation and reduction mechanisms of mobile dislocations have become balanced.
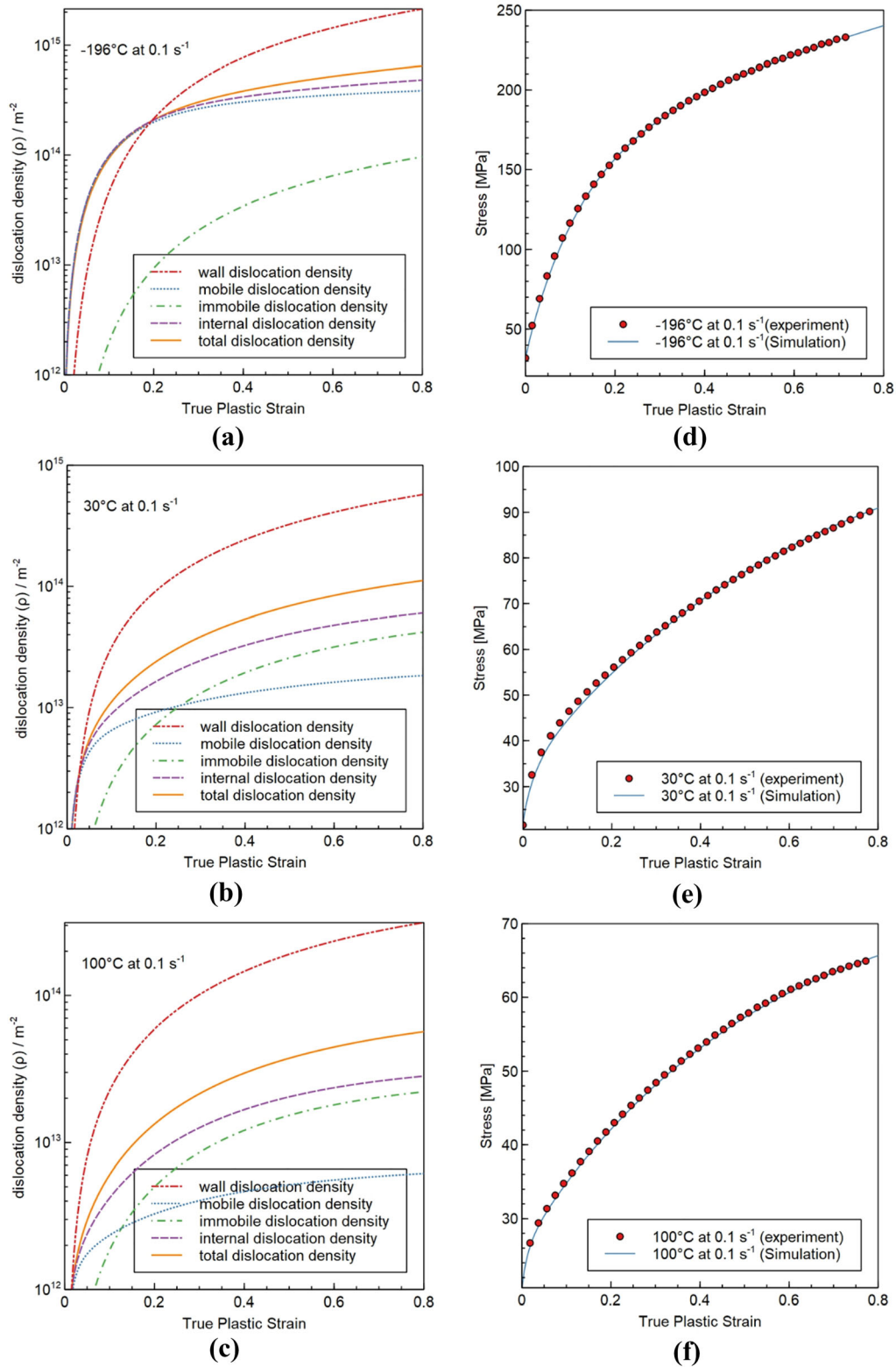
Fig. 6—Simulated dislocation densities during compression with rates of 0.1 s^{-1} at (*a*) − 196 °C, (*b*) 30 °C, and (*c*) 100 °C and comparison between experimental and simulated flow curves with rates of 0.1 s^{-1} at (*d*) − 196 °C, (*e*) 30 °C, and (*f*) 100 °C.

Similar to mobile dislocations, the generation of immobile and wall dislocations at the beginning of deformation is dominant. The reduction mechanisms become more prominent with the increase of the corresponding dislocation density. Figure 6 shows that the mobile dislocation density exhibits a much steeper
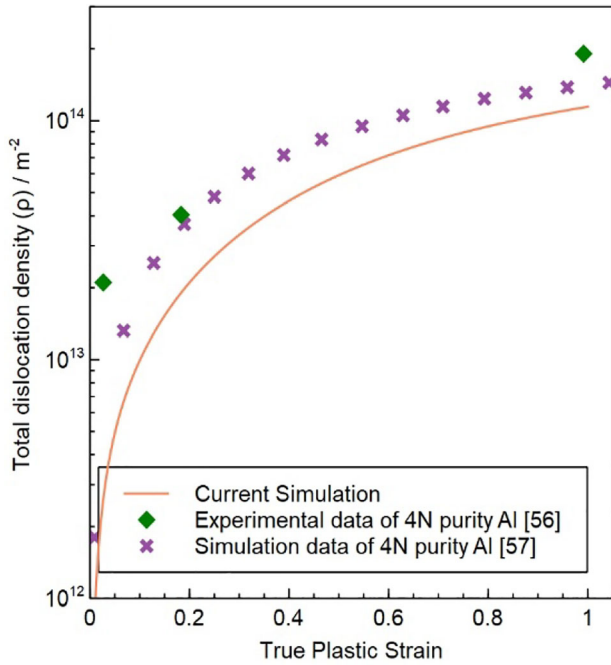
Fig. 7—Comparing the simulated dislocation density with the results from Gubicza et al.[65] and Chinh et al.[66].

Table III. Calibrated Functions for Pure Aluminum

Functions
$A_m = 494 - \frac{512{,}733}{T - 1.3\ln\dot{\varepsilon} + 10{,}551.6}$
$\beta_w = 1100$
$\beta_{fk} = -0.0007T + 0.0034\ln\dot{\varepsilon} + 0.65$
$B_m = 0.3927\exp(0.00788T - 0.07\ln\dot{\varepsilon}) + 0.663$
$A_{imm} = 0.0246\exp(0.0093T - 0.006\ln\dot{\varepsilon}) - 0.025$
$A_w = 0.0597\exp(0.0087T - 0.121\ln\dot{\varepsilon}) - 0.031$
$B_{imm} = 0.0743 - 0.00008T$
$B_w = -0.0013 + 0.00122T$
$C_m = 20$
$C_{imm} = 20$
$C_w = 20$
$\alpha_i = 0.34$
$\alpha_w = 0.34$

slope compared to the immobile and wall dislocation densities. This is because the reduction rate of immobile and wall dislocations is due to annihilation, whereas the reduction rate of mobile dislocations is due to both, annihilation and transformation into immobile or wall dislocations.

In the current model, mobile dislocations that form dipoles are considered to be the source of wall dislocations. An increasing wall dislocation density commonly goes hand in hand with a decreasing subgrain/cell size[49] and/or an increasing subgrain misorientation, which is in accordance with the results from Chakravarty et al.[67]

and Ito and Horita.[68] Interestingly, the calibrated simulations indicate that a lower amount of wall dislocations is generated at higher temperatures. One of the consequences is, therefore, a larger subgrain/cell size, in agreement with results from Chen et al.[69] and Ding et al.[70]

With increasing temperature, the probability of mobile dislocation interactions increases. Consequently, the ratio of mobile to total dislocations is lower and the ratio of wall to total dislocations is higher. At higher temperatures, the subgrain walls are formed earlier at less strain and lower internal dislocation density, in agreement with the findings of Chen et al.[69] and Ding et al.[70] Moreover, the athermal contribution to the strength of the material decreases with increasing temperature. From Taylor's equation, the dislocation density in the material should be lower at higher temperatures. As shown in Figure 6, at the end of deformation, the total dislocation density at 30 °C is about ten times lower than at − 196 °C. The mobile dislocation density is even roughly 30 times lower.

The evaluated dislocation densities simulate flow curves with an extended version of the Taylor equation (Eq. [2]). The effect of wall and internal dislocations on the strength, as controlled by the strengthening coefficients α_w and α_i, is accounted for equally with a value of 0.34.[71] The results from experimental flow curves show that the strain hardening rate is higher at the beginning of plastic deformation. This effect is well simulated in the current model and is attributed to the rapid increase in mobile dislocation density, in agreement with the results from Kreyca and Kozeschnik[18] and Sobotka et al.[72] These authors investigated the total dislocation density, whose generation rate determines the initial strain hardening. In the current work, mobile dislocations are generated first, and their generation controls the initial strain hardening.

According to Li et al.,[6] dynamic recrystallization at elevated temperatures reduces the strength of aluminum. This effect is observed in the present flow curves at 300 °C (Figure 8). At higher temperatures, dynamic recrystallization is less clearly seen, since the strength of the material is already very low, and static recovery and recrystallization significantly overlap. In the present simulations, dynamic recrystallization is not accounted for. Despite the effect of dynamic recrystallization, the simulated flow curves agree well with the experimental flow curves in all investigated stages of plastic deformation.

VI. CONCLUSIONS

The current work analyzes the evolution of dislocation densities during plastic deformation using an extended version of the classic 3IVM model. To make the model applicable also for larger strains, the annihilation of immobile and wall dislocations is accounted for based on the concept of the critical interaction volume. Compression tests on aluminum are performed and used
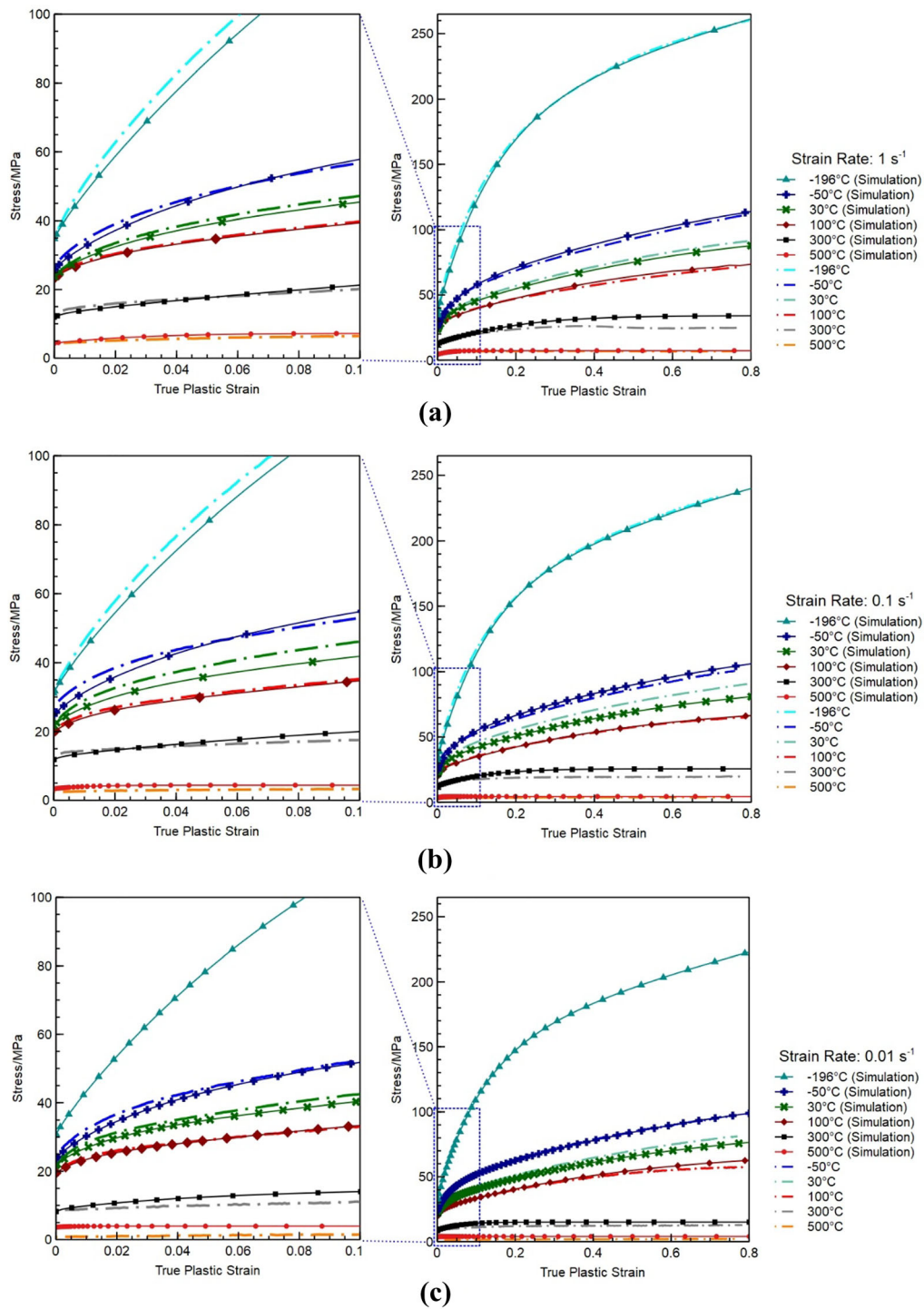
Fig. 8—Compression flow curves of pure aluminum (simulation and experiment) at different temperatures with an initial strain rate of (*a*) 1 s^{-1}, (*b*) 0.1 s^{-1}, and (*c*) 0.01 s^{-1}.

to calibrate the model parameters over a wide range of temperatures (−196 °C to 500 °C) and strain rates between 0.01 and 1 s^{-1}. With only a single set of model parameters, good agreement between simulated and experimental flow curves is achieved for all combinations of temperature and strain rate.

CONFLICT OF INTEREST

OPEN ACCESS

REFERENCES

1. N.Q. Chinh, J. Illy, Z. Kovács, Z. Horita, and T.G. Langdon: *Mater. Sci. Forum*, 2002, vol. 396–402, pp. 1007–12.
2. J.D. Bressan and K. Lopez: *Int. J. Mater. Form.*, 2008, vol. 1, pp. 213–16.
3. R. Schneider, R.J. Grant, N. Sotirov, G. Falkinger, F. Grabner, C. Reichl, M. Scheerer, B. Heine, and Z. Zouaoui: *Mater. Des.*, 2015, vol. 88, pp. 659–66.
4. H.R. Rezaei Ashtiani, M.H. Parsa, and H. Bisadi: *J. Mater. Sci. Eng. A*, 2012, vol. 545, pp. 61–67.
5. H. Pi, J. Han, C. Zhang, A.K. Tieu, and Z. Jiang: *J. Univ. Sci. Technol. Beijing*, 2008, vol. 15, pp. 43–47.
6. P. Li, F. Li, J. Cao, X. Ma, and J. Li: *Trans. Nonferr. Met. Soc. China*, 2016, vol. 26, pp. 1079–95.
7. L. Tabourot, M. Fivel, and E. Rauch: *J. Mater. Sci. Eng. A*, 1997, vol. 234–236, pp. 639–42.
8. U.F. Kocks: *J. Eng. Mater. Technol.*, 1976, vol. 98, pp. 76–85.
9. U.F. Kocks and H. Mecking: *Prog. Mater. Sci.*, 2003, vol. 48, pp. 171–273.
10. E.S. Puchi: *J. Eng. Mater. Technol.*, 1995, vol. 117, pp. 20–27.
11. M. Abo-Elkhier: *J. Mater. Eng. Perform.*, 2004, vol. 13, pp. 241–47.
12. A.S. Khan, J. Liu, J.W. Yoon, and R. Nambori: *Int. J. Plast.*, 2015, vol. 67, pp. 39–52.
13. D.J. Bammann: *Int. J. Eng. Sci. (Oxf. UK)*, 1984, vol. 22, pp. 1041–53.
14. E.B. Marin, D.J. Bammann, R.A. Regueiro, and G.C. Johnson: *Report No. SAND2006-0200*, Sandia National Laboratories, Livermore, 2006.
15. M.G. Lee, H. Lim, B.L. Adams, J.P. Hirth, and R.H. Wagoner: *Int. J. Plast.*, 2010, vol. 26, pp. 925–38.
16. T. Zhou, G. Wang, Y. Yang, Y. Li, and M. Shuai: *J. Mater. Eng. Perform.*, 2020, vol. 29, pp. 1262–71.
17. T. Hasegawa, Y. Sakurai, and K. Okazaki: *J. Mater. Sci. Eng. A*, 2003, vol. 346, pp. 34–41.
18. J. Kreyca and E. Kozeschnik: *Int. J. Plast.*, 2018, vol. 103, pp. 67–80.
19. B. Viernstein, T. Wojcik, and E. Kozeschnik: *Metals (Basel Switz.)*, 2022, vol. 12, p. 1207.
20. B. Viernstein, P. Schumacher, B. Milkereit, and E. Kozeschnik: *Minerals, Metals and Materials Series*, Springer, Berlin, 2020, pp. 267–71.
21. Y. Estrin and L.P. Kubin: *Acta Metall.*, 1986, vol. 34, pp. 2455–64.
22. L.P. Kubin and Y. Estrin: *Acta Metall. Mater.*, 1990, vol. 38, pp. 697–708.
23. F. Barlat, M.V. Glazov, J.C. Brem, and D.J. Lege: *Int. J. Plast.*, 2002, vol. 18, pp. 919–39.
24. B.L. Hansen, I.J. Beyerlein, C.A. Bronkhorst, E.K. Cerreta, and D. Dennis-Koller: *Int. J. Plast.*, 2013, vol. 44, pp. 129–46.
25. Y.Z. Li and M.X. Huang: *Int. J. Plast.*, 2021, vol. 138, p. 102921.
26. A. Arsenlis and D.M. Parks: *J. Mech. Phys. Solids*, 2002, vol. 50, pp. 1979–2009.
27. M. Goerdeler and G. Gottstein: *J. Mater. Sci. Eng. A*, 2001, vol. 309–310, pp. 377–81.
28. B. Glam, D. Moreno, S. Eliezer, and D. Eliezer: *AIP Conf. Proc.*, 2012, vol. 1426, pp. 987–90.
29. J. Fang, J. Mo, and J. Li: *Mater. Charact.*, 2017, vol. 129, pp. 88–97.
30. A. Rebhi, T. Makhlouf, J.P. Couzinié, Y. Champion, and N. Njah: *Mater. Sci. Forum*, 2011, vol. 667–669, pp. 451–56.
31. J. Gan, J.S. Vetrano, and M.A. Khaleel: *J. Eng. Mater. Technol.*, 2002, vol. 124, pp. 297–301.
32. M. Zehetbauer and V. Seumer: *Acta Metall. Mater.*, 1993, vol. 41, pp. 577–88.
33. M. Zehetbauer: *Acta Metall. Mater.*, 1993, vol. 41, pp. 589–99.
34. B. Holmedal, K. Marthinsen, and E. Nes: *Int. J. Mater. Res.*, 2005, vol. 96, pp. 532–45.
35. S. Kurukuri, A.H. van den Boogaard, A. Miroux, and B. Holmedal: *J. Mater. Process. Technol.*, 2009, vol. 209, pp. 5636–45.
36. G. Ji, Q. Li, K. Ding, L. Yang, and L. Li: *J. Alloys Compd.*, 2015, vol. 648, pp. 397–407.
37. V. Vilamosa, A.H. Clausen, T. Børvik, B. Holmedal, and O.S. Hopperstad: *Mater. Des.*, 2016, vol. 103, pp. 391–405.
38. K. Le Mercier, J.D. Guérin, M. Dubar, L. Dubar, and E.S. Puchi-Cabrera: *J. Alloys Compd.*, 2019, vol. 790, pp. 1177–91.
39. S. Saimoto, B.J. Diak, A. Kula, and M. Niewczas: *Acta Mater.*, 2020, vol. 198, pp. 168–77.
40. Z. Zhang, Z. Qu, L. Xu, R. Liu, P. Zhang, Z. Zhang, and T.G. Langdon: *Acta Mater.*, 2022, vol. 231, p. 117877.
41. E. Kozeschnik: *Encyclopedia of Materials: Metals and Alloys*, vol. 4, Elsevier, Oxford, 2022, pp. 521–26.
42. G.I. Taylor: *Proc. R. Soc. Lond. A*, 1934, vol. 145, pp. 362–87.
43. E. Orowan: *Z. Phys.*, 1934, vol. 89, pp. 605–13.
44. F. Roters, D. Raabe, and G. Gottstein: *Acta Mater.*, 2000, vol. 48, pp. 4181–89.
45. G.V.S.S. Prasad, M. Goerdeler, and G. Gottstein: *J. Mater. Sci. Eng. A*, 2005, vol. 400–401, pp. 231–33.
46. J. Kratochvíl and S. Libovický: *Scripta Metall.*, 1986, vol. 20, pp. 1625–30.
47. H. Zhang, X. Dong, D. Du, and Q. Wang: *J. Mater. Sci. Eng. A*, 2013, vol. 564, pp. 431–41.
48. A. Ma and F. Roters: *Acta Mater.*, 2004, vol. 52, pp. 3603–12.
49. E. Nes: *Prog. Mater. Sci.*, 1997, vol. 41, pp. 129–93.
50. J. Friedel: *Dislocations*, 1st ed. Pergamon Press Ltd., Oxford, 1964, pp. 116–69.
51. E. Orowan: *Proc. Phys. Soc.*, 1940, vol. 52, pp. 8–22.
52. D. Hull and D.J. Bacon: *Introduction to Dislocations*, 5th ed. Butterworth-Heinemann, Oxford, 2011, pp. 72–100.
53. R. Lagneborg, S. Zajac, and B. Hutchinson: *Scripta Metall. Mater.*, 1993, vol. 29, pp. 159–64.
54. L.E. Lindgren, K. Domkin, and S. Hansson: *Mech. Mater.*, 2008, vol. 40, pp. 907–19.
55. F.D. Fischer, J. Svoboda, F. Appel, and E. Kozeschnik: *Acta Mater.*, 2011, vol. 59, pp. 3463–72.
56. J.P. Hirth and J. Lothe: *Theory of Dislocations*, Krieger Publishing Company, Malabar, 1991.
57. E.I. Galindo-Nava, J. Sietsma, and P.E.J. Rivera-Díaz-Del-Castillo: *Acta Mater.*, 2012, vol. 60, pp. 2615–24.
58. H. Mecking, B. Nicklas, N. Zarubova, and U.F. Kocks: *Acta Metall.*, 1986, vol. 34, pp. 527–35.
59. M. Kato: *Introduction to the Theory of Dislocations*, Shokabo, Tokyo, 1999.
60. Y. Bergström: *Rev. Powder Metall. Phys. Ceram.*, 1983, vol. 2/3, pp. 79–265.
61. H.J. Frost and M.F. Ashby: *Deformation-Mechanism Maps: The Plasticity and Creep of Metals and Ceramics*, 1st ed. Pergamon Press, Oxford, 1982.

62. Z.D. Popovic, J.P. Carbotte, and G.R. Piercy: *J. Phys. F*, 1974, vol. 4, pp. 351–60.
63. S. Ghosh and P. Suryanarayana: *Mech. Res. Commun.*, 2019, vol. 99, pp. 58–63.
64. G. Ho, M.T. Ong, K.J. Caspersen, and E.A. Carter: *Phys. Chem. Chem. Phys.*, 2007, vol. 9, pp. 4951–66.
65. J. Gubicza, N.Q. Chinh, Z. Horita, and T.G. Langdon: *J. Mater. Sci. Eng. A*, 2004, vol. 387–389, pp. 55–59.
66. N.Q. Chinh, G. Horváth, Z. Horita, and T.G. Langdon: *Acta Mater.*, 2004, vol. 52, pp. 3555–63.
67. P. Chakravarty, G. Pál, and J.J. Sidor: *Mater. Charact.*, 2022, vol. 191, p. 112166.
68. Y. Ito and Z. Horita: *J. Mater. Sci. Eng. A*, 2009, vol. 503, pp. 32–36.
69. C.M. Chen, S.X. Ding, C.P. Chang, and P.W. Kao: *J. Mater. Sci. Eng. A*, 2009, vol. 512, pp. 126–31.
70. S.X. Ding, J.L. Lin, C.P. Chang, and P.W. Kao: *Metall. Mater. Trans. A*, 2006, vol. 37A, pp. 1065–73.
71. M. Sauzay and L.P. Kubin: *Prog. Mater. Sci.*, 2011, vol. 56, pp. 725–84.
72. E. Sobotka, J. Kreyca, M.C. Poletti, and E. Povoden-Karadeniz: *Materials*, 2022, vol. 15, p. 6824.